



Cite this: *J. Mater. Chem. C*, 2023, 11, 1311

# Raman spectra of 2D titanium carbide MXene from machine-learning force field molecular dynamics†

Ethan Berger, \*<sup>a</sup> Zhong-Peng Lv <sup>b</sup> and Hannu-Pekka Komsa <sup>a</sup>

MXenes represent one of the largest classes of 2D materials with promising applications in many fields and their properties are tunable by altering the surface group composition. Raman spectroscopy is expected to yield rich information about the surface composition, but the interpretation of the recorded spectra has proven challenging. The interpretation is usually done *via* comparison to the simulated spectra, but there are large discrepancies between the experimental spectra and the earlier simulated spectra. In this work, we develop a computational approach to simulate the Raman spectra of complex materials which combines machine-learning force-field molecular dynamics and reconstruction of Raman tensors *via* projection to pristine system modes. This approach can account for the effects of finite temperature, mixed surfaces, and disorder. We apply our approach to simulate the Raman spectra of titanium carbide MXene and show that all these effects must be included in order to appropriately reproduce the experimental spectra, in particular the broad features. We discuss the origin of the peaks and how they evolve with the surface composition, which can then be used to interpret the experimental results.

Received 14th October 2022,  
Accepted 10th December 2022

DOI: 10.1039/d2tc04374b

rsc.li/materials-c

## 1 Introduction

Two-dimensional (2D) materials have attracted a lot of attention from the scientific community in the last two decades. Among them, MXenes represent one of the largest classes of 2D materials with more than 40 synthesized compositions and many more still left to discover.<sup>1</sup> Due to their high electrical conductivity, MXenes show potential for applications in various fields, including energy storage, gas sensors, and electromagnetic interference shielding.<sup>2–4</sup> MXenes take the form  $M_{n+1}X_nT_x$ , where M is an early transition metal (*e.g.* titanium), X can be carbon or nitrogen, T is the surface terminations which depend on the synthesis methods, and  $n = 1–4$  defines the thickness of the layer. The first synthesized and the most studied MXene  $Ti_3C_2T_x$  is obtained by selective etching of the Al layer from its precursor bulk phase  $Ti_3AlC_2$ .<sup>5</sup> Due to this process, the surfaces are passivated by functional groups from the etching solution, with the most common ones being –O, –OH and –F. The ball-and-stick representations of pure –O and

–OH surfaces of  $Ti_3C_2$  are shown in Fig. 1(a and b), respectively. Under the common wet-etching synthesis conditions, the surface is never purely O or OH but contains a randomly arranged mixture of these functional groups.<sup>6–10</sup> Unfortunately, it has become challenging to not only control the ratio of these terminations, but also to quantify them.

One commonly used method to study the composition of 2D materials is Raman spectroscopy, which is a non-destructive method for characterizing the vibrational properties of molecules or solids. The Raman spectra of  $Ti_3C_2T_x$  have been recorded and carefully studied experimentally.<sup>11–13</sup> To explain the experimental observations, Raman spectra have been calculated using density functional theory (DFT) for pure surfaces,<sup>14,15</sup> but the comparison is not straightforward. To illustrate these problems, in Fig. 1(c), we reproduce the typical experimental Raman spectrum and the frequencies of the Raman active modes of pure surfaces (–O and –OH) from DFT (the description of the synthesis and the Raman measurement for the experimental results are available in the ESI†). For modes around  $120\text{ cm}^{-1}$ ,  $200\text{ cm}^{-1}$ , and  $700\text{ cm}^{-1}$ , the experimental frequencies appear to be close to, or in between, those of the calculations for pure surfaces, and thus these peaks can be quite safely assigned to the calculated modes. More importantly, other peaks at around  $300–400\text{ cm}^{-1}$  and  $600\text{ cm}^{-1}$  show extremely broad features which cannot be explained by static calculations of pure surfaces. There are

<sup>a</sup> Microelectronics Research Unit, Faculty of Information Technology and Electrical Engineering, University of Oulu, P. O. Box 4500, Oulu, FIN-90014, Finland.  
E-mail: hannu-pekka.komsa@oulu.fi

<sup>b</sup> Department of Applied Physics, Aalto University, Aalto, FIN-00076, Finland

† Electronic supplementary information (ESI) available. See DOI: <https://doi.org/10.1039/d2tc04374b>



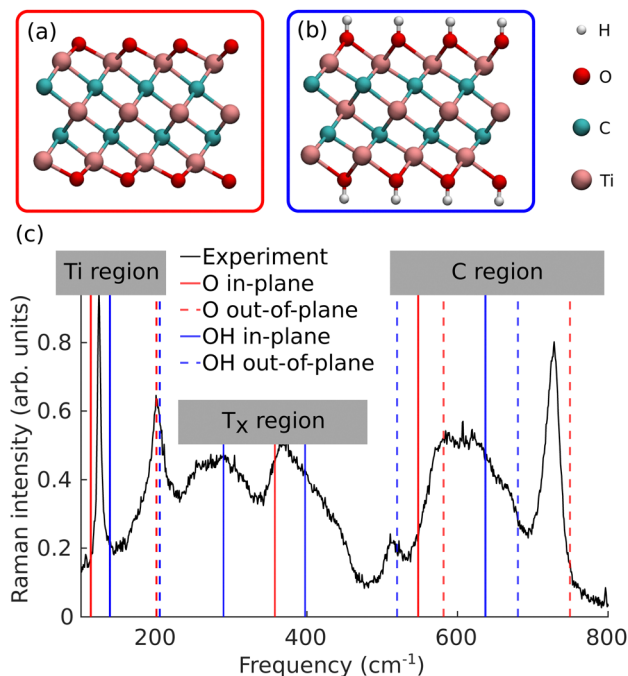


**Fig. 1** (a and b) Ball-and-stick representation of pure  $\text{Ti}_3\text{C}_2\text{O}_2$  and  $\text{Ti}_3\text{C}_2(\text{OH})_2$ , respectively. Titanium is in pink, carbon in blue, oxygen in red and hydrogen in white. (c) Experimental Raman spectrum of  $\text{Ti}_3\text{C}_2\text{Tx}$  compared with the frequencies of the Raman active modes calculated using DFT. The red and blue lines correspond to the calculations of pure  $\text{Ti}_3\text{C}_2\text{O}_2$  and pure  $\text{Ti}_3\text{C}_2(\text{OH})_2$ , respectively. The full lines represent the in-plane modes while the dashed ones represent the out-of-plane modes.

few possible origins for this discrepancy. First, static calculations do not provide any information about the width of the Raman peaks. The calculations of anharmonic interatomic force constants<sup>16</sup> or molecular dynamics (MD) simulations are usually necessary to account for temperature effects and obtain realistic line widths. In the latter, Raman intensities can be obtained from the Fourier transform of the polarizability  $\chi(t)$  autocorrelation function,<sup>17</sup> but this requires tens of thousands of polarizability calculations. It has been successfully used to compute the Raman spectra of solid ice,<sup>18</sup> liquid water,<sup>19</sup> and molecules,<sup>20</sup> but such calculations are very expensive and usually restricted to a small number of atoms. Secondly, wide peaks of the MXene Raman spectra might come from the structural disorder, *i.e.*, the mixed surfaces. In order to simulate different surface terminations, it is necessary to use a large supercell, making the calculation of polarizabilities at every time step of an MD run computationally intractable.

With the recent developments in machine-learning force fields (MLFFs), it has now become possible to carry out MD simulations for long times and large numbers of atoms efficiently, yet still nearly matching the accuracy of first-principles calculations.<sup>21–26</sup> Moreover, by using MLFFs, it becomes possible to run MD over a large configurational space, such as different compositions and distributions of surface terminations in MXenes. Unfortunately, MLFFs usually cannot be used to evaluate polarizabilities as they only model energies and forces. To compute the polarizabilities of these large supercells,

Hashemi *et al.* recently developed a computational scheme (denoted as RGDOS), which allows the Raman tensors of a supercell to be obtained from a projection onto those of the unit cell.<sup>27</sup> The scheme has already been successfully applied to, *e.g.*, transition metal dichalcogenide alloys ( $\text{Mo}_x\text{W}_{1-x}\text{S}_2$  and  $\text{ZrS}_x\text{Se}_{1-x}$ ),<sup>27,28</sup> defects in  $\text{MoS}_2$ ,<sup>29</sup> and  $\text{SnS}$  multilayer films.<sup>30</sup> Adapting RGDOS for evaluating the time-dependent polarizability  $\chi(t)$  and combining it with MLFF MD trajectories would lead to a highly efficient scheme to obtain the Raman spectra at a finite temperature and in large supercells. In this work, we present a scheme for combining MLFF trajectories with RGDOS (or DFT calculated Raman tensors) to evaluate the finite-temperature Raman spectra of complex systems. This method leads to highly efficient MD runs and calculations of the polarizabilities, allowing us to easily probe the large configurational space. We apply the method to 2D titanium carbide MXene to study the effect of heterogeneous surfaces on the Raman spectra and attempt to give a better description of the experimental results. We first investigate the effects of temperature and mixed surface terminations on the Raman spectrum, and finally study the effect of additional disorder by considering the vibrational modes outside a  $\Gamma$ -point. We discuss the origin of the peaks and broad features and how they evolve with the surface composition.

## 2 Methods

When using MD, the Raman spectrum is obtained as the Fourier transform of the autocorrelation function of polarizability  $\chi$ :<sup>17,31</sup>

$$I(\omega) = \int \langle \chi(\tau)\chi(t+\tau) \rangle_{\tau} e^{-i\omega t} dt \quad (1)$$

where  $\langle x(\tau)x(t+\tau) \rangle_{\tau}$  denotes the autocorrelation function. Therefore, the challenge is how to obtain the polarizability of a large supercell for every configuration visited during MD at a reasonable computational cost. In RGDOS,<sup>27</sup> the Raman tensors of a large supercell are obtained by first projecting its vibrational modes onto those of the pristine unit cell and then combining the Raman tensors of the unit cell weighted with these projections. This means that only the Raman tensors of the unit cell have to be calculated, resulting in an immense reduction of computational effort. This scheme has already been successfully applied to study the effect of alloys, defects, and film thicknesses on the Raman spectra, all involving large supercells.<sup>27–30</sup> Since this method does not rely on the electronic structure of the supercell, it is perfectly suited to be used with empirical or MLFF MD simulations. Moreover, when combined with MD simulations, such a method would also account for temperature effects and anharmonicity.

In this work, we adopt an approach conceptually similar to the RGDOS. We start by writing the polarizability as a Taylor expansion around a relaxed position  $\mathbf{r}_0$ , which leads to the following equation where  $\chi_0$  is the polarizability at  $\mathbf{r}_0$  and  $\mathbf{u}$



represents the atomic displacement

$$\chi(\mathbf{u}) = \chi_0 + \frac{\partial \chi}{\partial \mathbf{u}} |\mathbf{u}| + O(|\mathbf{u}|^2). \quad (2)$$

One can notice the resemblance between the partial derivative  $\frac{\partial \chi}{\partial \mathbf{u}}$  and the definition of Raman tensors  $R_m = \frac{\partial \chi}{\partial \mathbf{e}_m^*}$  (in the Placzek approximation<sup>32,33</sup>), where  $\mathbf{e}_m^*$  are the mass-scaled eigenvectors of the unit cell. This suggests that we could use the set of eigenvectors  $\{\mathbf{e}_m^*\}$  as a basis for the expansion, with Raman tensors giving the expansion coefficients and the “distance” given by the projection of  $\mathbf{u}$  to  $\mathbf{e}_m^*$ , written as

$$\frac{\partial \chi}{\partial \mathbf{u}} |\mathbf{u}| = \sum_m R_m P_m(\mathbf{u}). \quad (3)$$

where  $P_m(\mathbf{u})$  is the projection of  $\mathbf{u}$  onto  $\mathbf{e}_m^*$ . We first note that, since eigenvectors  $\{\mathbf{e}_m^*\}$  do not form an orthogonal basis, the projection coefficients  $P_m(\mathbf{u})$  have to be found by solving the following system of linear equations

$$\sum_i \langle \mathbf{e}_m^* | \mathbf{e}_i^* \rangle P_i(\mathbf{u}) = \langle \mathbf{e}_m^* | \mathbf{u} \rangle. \quad (4)$$

Moreover, since only  $\Gamma$ -point modes contribute to first-order Raman scattering, the projections are here performed from the supercell displacement  $\mathbf{u}$  to the unit cell eigenmodes at  $\Gamma$ -point  $\mathbf{e}_m^*$ .

The final equation for the time-dependent polarizability is then

$$\chi(t) = \chi(\mathbf{u}(t)) = \chi_0 + \sum_m R_m P_m(\mathbf{u}(t)). \quad (5)$$

When the eigenmodes and the Raman tensors of the unit cell and the MD trajectories are known,  $\chi(t)$  can easily be obtained from eqn (4) and (5). This method is therefore highly efficient and compatible with MLFF MD. We also note that in eqn (5), the second order term could be added, essentially corresponding to the second-order Raman scattering. In this case, the sum should also be carried over different points of the first Brillouin zone (BZ) to account for the modes outside of the gamma-point. In the case of MXenes, there is no indication of the dominant second order contribution and thus we have decided not to include the second order term.

### 3 Computational details

All calculations are performed using the Vienna *ab initio* simulation package (VASP).<sup>34,35</sup> We adopt the Perdew–Burke–Ernzerhof exchange–correlation functional for solids (PBEsol)<sup>36</sup> and set the plane-wave cutoff to 550 eV. Phonon eigenmodes are obtained using the Phonopy software.<sup>37</sup> For determining the force constants, we used  $4 \times 4$  supercells with the Brillouin zone sampled using a  $4 \times 4$   $k$ -point mesh. Once the eigenvectors are known, the Raman tensors were obtained from a centered finite difference scheme. Since MXenes are metallic, the polarizabilities have to be evaluated at a finite excitation energy  $\omega$ , *i.e.*, using  $\chi(\omega)$  instead of the  $\omega \rightarrow 0$  limit normally

used in nonresonant Raman. Although the Placzek approximation is derived under non-resonant conditions, it has been found to work well also under resonant conditions.<sup>38</sup> Here, for the projections, we used the eigenvectors and Raman tensors of the –OH unit cell, and the latter evaluated at  $\omega = 516$  nm. More information regarding resonant Raman and the choice of Raman tensors is available in the ESI† (see in particular Fig. S1). The frequency-dependent polarizability (or the dielectric function) is computed using a summation over empty bands.<sup>39</sup> To guarantee the accurate evaluation of small changes in  $\chi(\omega)$ , a denser  $k$ -point mesh of  $48 \times 48$  (in the unit cell) was adopted and the number of orbitals was increased to 120 (roughly 4 times the recommended amount). For phonon mode and Raman tensor calculations, the electronic structure was relaxed with a precision of  $10^{-7}$  eV.

The machine learning force field (MLFF) was trained using on-the-fly machine learning, as recently implemented in VASP.<sup>25,26</sup> This method is based on the Gaussian approximation potential (GAP)<sup>23</sup> and has already been successfully applied to different materials including different phases of zirconium<sup>40</sup> and hybrid perovskites MAPbX<sub>3</sub>.<sup>41,42</sup> A detailed presentation of the method as well as definitions of descriptors and the kernel can be found in ref. 26. Fig. 2(a) shows a schematic of the workflow and how the MLFF, MD, DFT and RG DOS are all combined to obtain the Raman spectrum. In the training, we again used  $4 \times 4$  supercells with a  $4 \times 4$   $k$ -points mesh, but the electronic structure convergence criterion was decreased to  $10^{-4}$  eV. The model was first trained for pure surfaces before being trained for mixed –O and –OH surfaces as well. F- and OH-terminated surfaces are expected to behave fairly similar chemically,<sup>10,43,44</sup> and also for vibrational frequencies due to similar masses.<sup>45</sup> On a practical level, the MLFF applicable to any mixed surfaces containing O, OH or F would have to be trained with a much larger number of surface compositions, which would be computationally costly in both the training stage and the MD runs. We carried out benchmarks using a model trained with few F compositions (see the ESI† and Fig. S2 in particular), which confirm our initial assumption that replacing –OH terminations by –F is found to have fairly little impact on the Raman spectra. Hence –F terminations are not included in the MLFF model used in the main text. Each step consisted of MD simulation in the NVT ensemble at 300 K for 20 hours (40 000–70 000 steps), and the MLFF configurations after each step carried on to the next step. In total, the training set contains 1364 configurations. During on-the-fly training, weights are calculated using Bayesian linear regression, which is necessary for error estimates. Once training is performed, the final model is retrained using singular value decomposition (SVD), which usually improves the quality of the MLFF. During training and retraining, we use 8 basis functions, a cutoff radius of 5 Å and a Gaussian broadening of 0.5 Å to build both radial and angular descriptors (these values correspond to the default parameters of VASP, see ref. 26 for a detailed definition of the descriptors).

To benchmark the model, we compared the phonon dispersion curves from DFT and the MLFF model. Fig. 2(b and c)



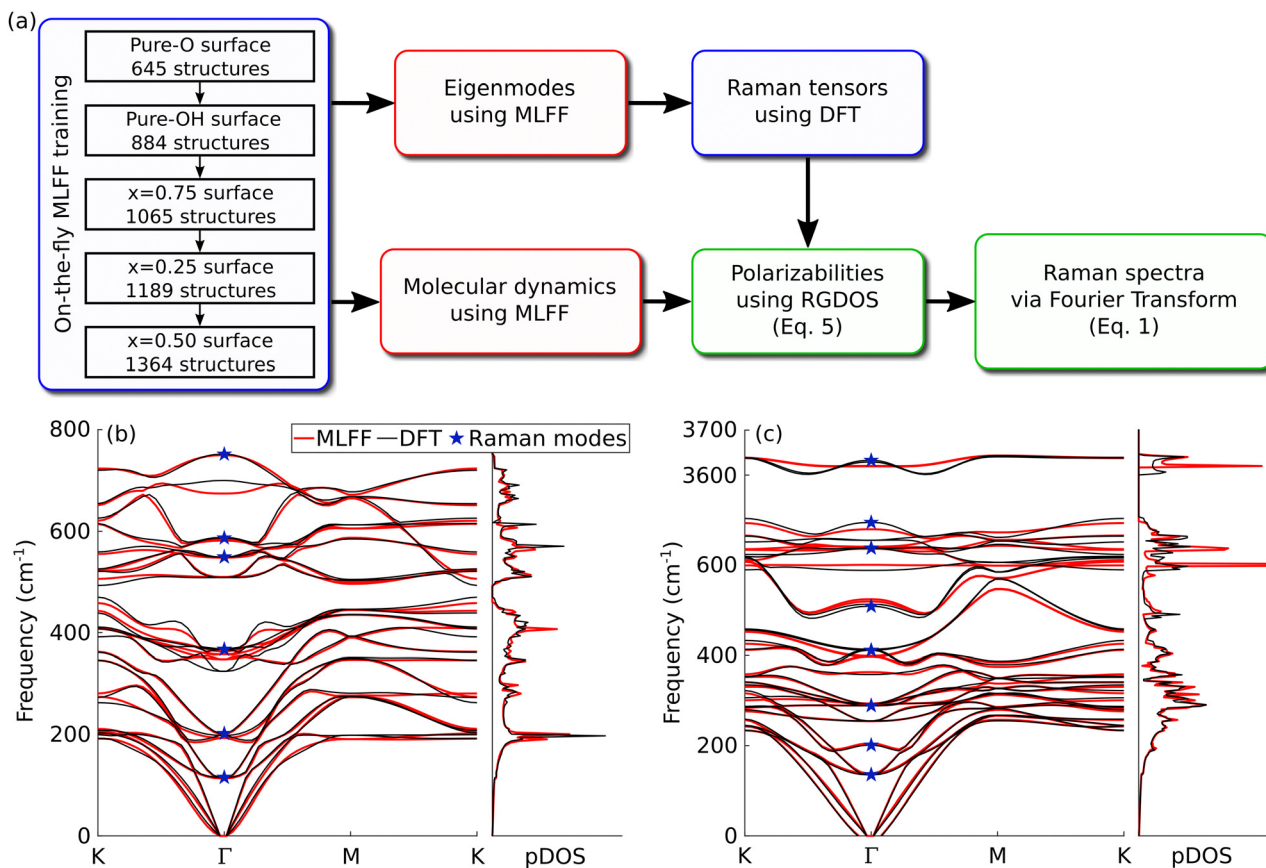


Fig. 2 (a) Schematic workflow of the computational approach. The blue boxes represent steps using DFT calculations, the red boxes represent steps using MLFF, and the green boxes are post-processing steps. (b and c) Phonon dispersion curves and density of states (pDOS) of  $\text{Ti}_3\text{C}_2\text{O}_2$  and  $\text{Ti}_3\text{C}_2(\text{OH})_2$ , respectively. The results from MLFFs (red lines) are compared with those from DFT (black lines). The blue stars indicate Raman-active modes at  $\Gamma$ -point.

show the phonon bands and density of states (pDOS) of pure  $\text{Ti}_3\text{C}_2\text{O}_2$  and  $\text{Ti}_3\text{C}_2(\text{OH})_2$ , respectively. Overall, the results are in good agreement with the dispersion curves and the pDOS. The bands of  $\text{Ti}_3\text{C}_2\text{O}_2$  are in great agreement. Fortunately, few modes where errors at  $\Gamma$ -point are somewhat larger, such as the 350 and 700  $\text{cm}^{-1}$  modes in  $\text{Ti}_3\text{C}_2\text{O}_2$ , happen to be Raman-inactive modes. The comparison for  $\text{Ti}_3\text{C}_2(\text{OH})_2$  is slightly worse. In particular, modes in the 400–700  $\text{cm}^{-1}$  range show deviations that are larger than those in  $\text{Ti}_3\text{C}_2\text{O}_2$ , but generally still within about 20  $\text{cm}^{-1}$  and with largely correct band dispersions. We also note that part of the discrepancy may be ascribed to the fact that phonon dispersion curves are calculated around the equilibrium positions, essentially corresponding to spectra at 0 K, whereas our MLFF is fitted into finite-temperature trajectories, *i.e.*, aimed at yielding accurate forces at room temperature. This becomes particularly true for light elements such as hydrogen and might explain the larger errors in  $\text{Ti}_3\text{C}_2(\text{OH})_2$  phonon dispersion curves. The effect of temperature is further discussed below. The root mean square error (RMSE) between DFT and MLFF forces is 45.8  $\text{meV } \text{\AA}^{-1}$ . These benchmarks indicate that the model is sufficiently trained and that we can use it for reliable MD production runs.

Molecular dynamics were performed using the MLFF model in the NVT ensemble using a Nosé–Hoover thermostat<sup>46,47</sup> for

$8 \times 8$  supercells (see Fig. S3(a) in the ESI† for a discussion on the choice of supercell size). The time step was set to 1 fs and  $10^5$  steps were performed, resulting in runs of 100 ps. To reduce noise in the final spectra, five runs with different random distributions of the surface terminations are performed for each concentration. Using different distributions of the surface termination does not impact the main features of the resulting Raman spectra, see Fig. S3(b) in the ESI† for more details.

## 4 Results and discussion

### 4.1 Effect of temperature

We first investigate the effect of temperature on the width of the peaks. Fig. 3(a and b) show the Raman spectra of  $\text{Ti}_3\text{C}_2\text{O}_2$  and  $\text{Ti}_3\text{C}_2(\text{OH})_2$  at different temperatures, respectively. With the MLFF being trained at 300 K, MD runs were only performed at lower temperatures of 100 K and 200 K as trajectories for temperatures above 300 K might not be reliable. For a better understanding of the different vibrations, Fig. 3(c) shows a representation of the Raman-active modes. The peak frequencies compare well to the DFT results presented in Fig. 1(c) for both systems, showing that our approach leads to reasonable spectra. Overall, the frequencies do not shift markedly with







**Fig. 3** (a and b) Raman spectra at different temperatures of  $\text{Ti}_3\text{C}_2\text{O}_2$  and  $\text{Ti}_3\text{C}_2(\text{OH})_2$ , respectively. The blue lines represent the in-plane modes while the red ones represent the out-of-plane modes. The grey areas show the experimental results and the dashed vertical lines show the frequencies from phonon calculations using the MLFF. (c) Eigenmodes of Raman active modes.

temperature, but there is now a realistic description of the peak widths. Some peaks, such as the two modes at 100 and 200  $\text{cm}^{-1}$  localized to titanium atoms, show weak dependence on temperature. While our results agree with experimental observations for the first, the width seems underestimated for the latter. For other peaks, the width increases with temperature. The  $A_{1g}$  carbon mode at around 700  $\text{cm}^{-1}$  shows a fairly narrow peak at a low temperature but it gets significantly wider with temperature, resulting in a better agreement with experiment at 300 K. Similar broadening with increasing temperature

is observed for the in-plane modes of surface terminations and carbon at 300–400 and 500–600  $\text{cm}^{-1}$ , respectively. Since surface terminations ( $-\text{OH}$  groups in particular) should be strongly anharmonic, significant broadening could be expected for modes involving these atoms. In these cases however, the widths at 300 K are still underestimated and do not compare well to experiments. Overall, using finite temperature leads to a better comparison with experiments, but it is clear that something is still missing in order to correctly reproduce experimental observations.

## 4.2 Effect of mixed surfaces

We next look at the effect of mixed surfaces. Fig. 4(a) shows the Raman spectra for different concentrations of surface terminations and Fig. 4(b) shows the distribution of surface terminations for different concentrations. The top and bottom lines show the results of pure  $\text{Ti}_3\text{C}_2\text{O}_2$  and  $\text{Ti}_3\text{C}_2(\text{OH})_2$ , respectively. The titanium  $A_{1g}$  mode at 200  $\text{cm}^{-1}$  is largely unaffected by the composition changes. The other two sharp peaks from both the titanium  $E_g$  mode at around 120  $\text{cm}^{-1}$  and the carbon  $A_{1g}$  mode at around 700  $\text{cm}^{-1}$  show a straightforward linear shift with the O/OH ratio (a so-called one-mode behavior). This suggests that these peaks could be used to find the surface termination composition from the experimentally recorded spectrum. To this end, we extracted the frequencies by isolating the peaks and fitted them using a Lorentzian function (see Fig. S4 in the ESI† for details), and collected the results in Table 1 together with experimental values. In particular, we include the results from our experimental spectrum shown in Fig. 1(c) (and again in Fig. 4(a) below the  $x = 0.625$  spectrum) and those from ref. 11, where these peaks were found to shift depending on the sample preparation conditions. First, if we use the Ti  $A_{1g}$  mode as a probe for the accuracy of our calculations, we find that the calculated frequencies are 0–10  $\text{cm}^{-1}$  lower than the experimental values. Second, by comparing the frequencies of the other two modes, best agreement with experiments is found for  $x$  around 0.5–0.625. Even accounting for the inaccuracies in the calculated frequencies, our results strongly point to all these samples having surfaces with a mixture of surface terminations. Interestingly, the composition range found from this comparison also agrees well with that predicted by first-principles calculations in ref. 9:  $\text{O}_{0.75}\text{OH}_{0.25}$  ( $x = 0.75$ ) at a higher pH and  $\text{O}_{0.5}\text{OH}_{0.25}\text{F}_{0.25}$  at a lower pH (corresponding to a total concentration of 0.5 for  $-\text{OH}$  and  $-\text{F}$  terminations). For these two peaks, calculations also reproduce well the widths of the experimental peaks.

In addition, there are two in-plane modes at 300–400  $\text{cm}^{-1}$  and 500–650  $\text{cm}^{-1}$ , which show distinct two-mode behavior with changing composition. For the former, it seems that the two broad features in the experimental spectrum arise from these two modes. For the latter, it is difficult to distinguish the two peaks from the experimental spectrum, but as this feature is very broad it is consistent with being composed of two peaks as found in our calculations. Also note that at concentrations close to  $x = 0.5$ , the out-of-plane mode of carbon also seems to contribute at a similar frequency. Even though Raman spectra simulated using mixed surfaces agree much better with

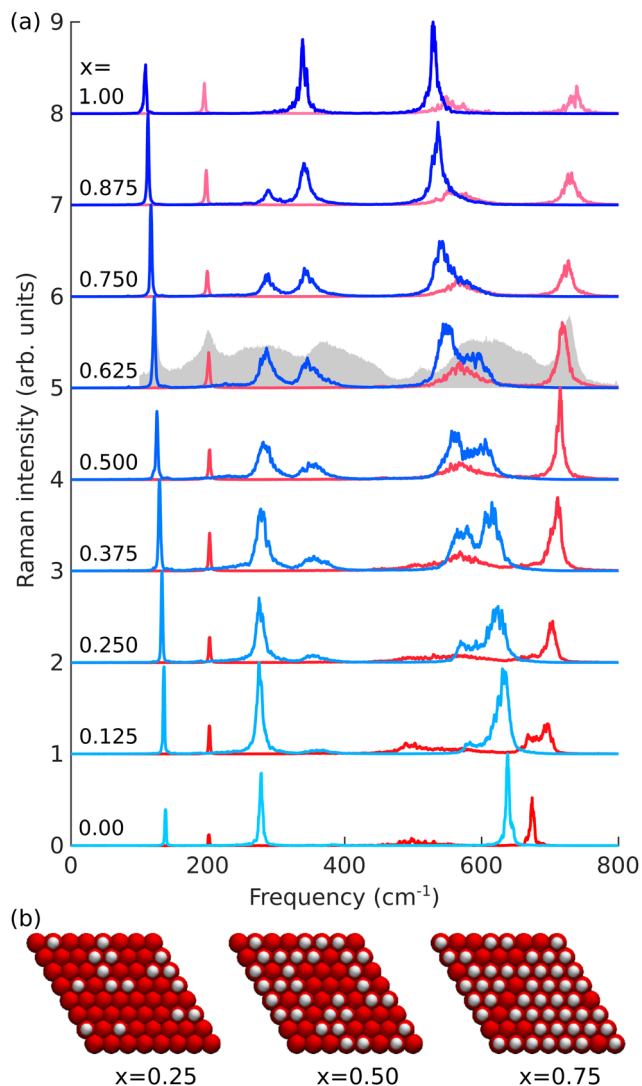


Fig. 4 (a) Raman spectra of  $\text{Ti}_3\text{C}_2(\text{O}_x\text{OH}_{1-x})_2$  for different surface group compositions. Labels on the left show the concentration of oxygen at the surface, e.g. the top and bottom lines represent pure  $-\text{O}$  and  $-\text{OH}$  surfaces, respectively. In-plane modes are represented by the blue lines while out-of-plane modes are represented by the red lines. The grey areas show the experimental observation for comparison. (b) Top view of the surface structure of  $\text{Ti}_3\text{C}_2(\text{O}_x\text{OH}_{1-x})_2$  for  $x = 0.25, 0.5$  and  $0.75$  (only shown one of the five configurations averaged over). The distribution of surface terminations is random and the red balls show  $-\text{O}$  sites while the white ones show  $-\text{OH}$  sites.

experiments and would appear to contain all the main features, the agreement is clearly still far from perfect. In particular,

the widths of some peaks, mainly those arising from the surface terminations and the carbon  $E_g$  modes, are still greatly underestimated even when accounting for the F terminations (Fig. S2, ESI†) and by more than one might expect from instrumental broadening.

### 4.3 Effect of modes outside the $\Gamma$ -point

The peak broadening could arise from the interaction of surface terminations with water or other surface adsorbates, from the interaction with neighboring MXene layers, or from disorder arising, e.g., from point defects, grain boundaries, etc. We simulated the Raman spectra of multilayer MXene flakes, but this did not lead to marked broadening of these features as shown in Fig. S5(a) in the ESI†. Moreover, the experimentally recorded spectra of monolayer flakes, multilayer flakes, and colloidal dispersions all show largely similar broadening.<sup>11–13</sup> We also investigated the presence of (a small amount of) water on the surface, but it also did not yield the desired effect (see Fig. S5(b) in the ESI†).

One might expect that the wet chemistry and strong acids used in the synthesis would lead to a large number of defects, in addition to the defects inherited from the precursor MAX phases.<sup>48–50</sup> Consequently, there is also a large variety of possible defects: in addition to flake edges and grain boundaries,<sup>2,48,51</sup> the reported point defects include Ti vacancies and Ti adatoms,<sup>52,53</sup> C vacancies,<sup>54</sup> and substitutional O in the C site.<sup>55</sup> Recent secondary-ion mass-spectroscopy measurements have revealed that this last kind of defect can occupy up to 30% of the carbon sites, confirming the high defect concentration in the interior of MXenes.<sup>56</sup> Unfortunately, the dominant types of defects and their density are largely unknown, which makes simulating the role of defects on the Raman spectra challenging.

To circumvent this problem, we simulate the effect of disorder by considering the modes outside the  $\Gamma$ -point. In ideal crystals, first order Raman spectra only come from modes at  $\Gamma$ -point because of the condition  $k = 0$ .<sup>57</sup> However, in the presence of defects, the symmetry is lowered and the modes from the rest of the first Brillouin zone can contribute.<sup>58,59</sup> In fact, this effect is already present in our calculations for randomly distributed surface terminations, but clearly the degree of disorder from surface terminations is insufficient. To explicitly include the contributions from modes outside the  $\Gamma$ -point, we study here the phonon density of state using the phonon-projected velocity-autocorrelation function (VACF).<sup>42,60–62</sup> By projecting only onto the Raman active modes, we can isolate the corresponding part of the vibrational spectrum and in this

**Table 1** Frequencies (in  $\text{cm}^{-1}$ ) of the  $E_g$  (Ti),  $A_{1g}$  (Ti), and  $A_{1g}$  (C) modes for different ratios of O/OH surface terminations, and comparison to experimental values

	Simulated									Experiments	
	1.000	0.875	0.750	0.625	0.500	0.375	0.250	0.125	0.000	Fig. 1	Ref. 11
$E_g$ (Ti)	108.4	112.5	116.8	121.6	125.7	129.3	132.9	135.7	138.1	123.7	119.8–124.5
$A_{1g}$ (Ti)	194.9	197.7	199.2	200.3	202.3	202.6	202.5	202.3	201.5	199.6	201.0–206.7
$A_{1g}$ (C)	737.4	729.4	725.2	718.9	714.5	709.9	702.0	690.2	673.9	728.3	737.7–719.6

way approximate the Raman spectrum. Note however that the peak intensities do not correspond to those obtained from Raman and only the frequencies and lineshapes are relevant. The comparison to the total pDOS (*i.e.* containing both infrared and Raman active modes) is presented in the ESI† (see Fig. S6).

We focus here on  $x = 0.5$  surfaces since we already determined this concentration as a good candidate to reproduce the experimental results. Every point of the reciprocal space is not expected to contribute to the Raman spectra with the same weight. To find the weights, we study the pDOS for each wave vector along the  $\Gamma$ -M path, which are shown in Fig. 5(a). pDOS at and close to  $\Gamma$  mostly show low frequency modes, coinciding with the Raman spectrum in Fig. 4. In experiment, these modes show narrow peaks which tends to indicate a small contribution from modes outside the  $\Gamma$  point. On the other hand, modes close to the edge of the first Brillouin zone show wide peaks at around 300–400 and 600  $\text{cm}^{-1}$ . Based on the experimental observations, we therefore choose larger weights for the modes close to the BZ edges. The selected weights are shown in Fig. 5(b) and built from a sum of two Gaussians such that the weight approaches 0 at  $\Gamma$ -point and 1 at the BZ edge, except that the pDOS at  $\Gamma$ -point is also added with a weight of 1.

The resulting pDOS using these weights is shown in Fig. 5(c). When summing the weighted pDOS with pDOS at  $\Gamma$ , we found great agreement with experiment. The very wide peaks in the 300–400 and 600  $\text{cm}^{-1}$  regions are well

reproduced. The peak at 200  $\text{cm}^{-1}$  also gets wider with the additional contributions from outside  $\Gamma$ , further improving the agreement with experiment. As previously discussed, the pDOS does not reproduce well the intensities of peaks, which is especially true for the peak at 700  $\text{cm}^{-1}$ . Also note that the spectrum now shows an additional peak at around 500  $\text{cm}^{-1}$  which also appears in the experimental results, even though the agreement in the frequency is not perfect. In Fig. 4(a), this peak shows up weakly in the OH-surfaces, but disappears in the mixed surfaces. However, since this mode is relatively flat [*cf.* the phonon dispersion in 2(c)], the inclusion of modes outside the  $\Gamma$ -point could lead to increased intensity. Thus, this peak seems to arise from the  $A_{1g}$  (OH) mode with its intensity enhanced by disorder, which we could confirm by inspecting the eigenmode-projected VACF in Fig. S6(b) in the ESI.†

Similar pDOS for other concentrations is available in the ESI† (Fig. S7). The results in Fig. S7 (ESI†) and those in Fig. 4 suggest that the relative intensity of the two broad peaks at 300  $\text{cm}^{-1}$  [ $E_g$  (OH)] and 400  $\text{cm}^{-1}$  [ $E_g$  (O)] and of the two peaks that form the broad peak at 600  $\text{cm}^{-1}$  [ $E_g$  (C)] could be used to probe the O/OH concentration, in addition to the shift of the sharp peaks. In fact, our results are in agreement with all the changes with increasing O content (as verified using XPS) observed in the experiments by Lioi *et al.*:<sup>12</sup> for the sharp peaks, there is a downshift of 120  $\text{cm}^{-1}$  [ $E_g$  (Ti)] peak, a downshift of 200  $\text{cm}^{-1}$  [ $A_{1g}$  (Ti)] peak, and an upshift of 700  $\text{cm}^{-1}$  [ $A_{1g}$  (C)] peak; for the broad features, there is enhancement of the 400  $\text{cm}^{-1}$  [ $E_g$  (O)] peak and enhancement of the lower frequency side of the 600  $\text{cm}^{-1}$  peak. Only 500  $\text{cm}^{-1}$  [ $A_{1g}$  (OH)] does not show a marked change. The results in Fig. S7 (ESI†) also illustrate that the surface concentration has a relatively minor impact on these peaks. This finding, together with previous computational predictions of a limited range of accessible surface compositions under typical synthesis conditions,<sup>9</sup> explains why the Raman spectra of  $\text{Ti}_3\text{C}_2\text{T}_x$  appear to depend weakly on the adopted synthesis procedure and on the sample morphology.

## 5 Conclusion

In conclusion, we have developed a computational approach to efficiently compute the Raman spectra of complex materials at a finite temperature, which is based on a combination of machine-learning force fields and a method to efficiently evaluate the time-dependent susceptibility. Our approach can be applied to many other materials with high anharmonicity and pronounced temperature effects. Alternatively, it can be used for systems requiring large supercells when modeling, *e.g.*, alloys and/or defects.

Here, we applied the approach to 2D titanium carbide MXene to study the effects of temperature and surface terminations on the Raman spectra. We found that the temperature plays a relatively small role and does not explain the wide peaks observed experimentally. On the other hand, mixed surfaces play an important role in reproducing the experimental

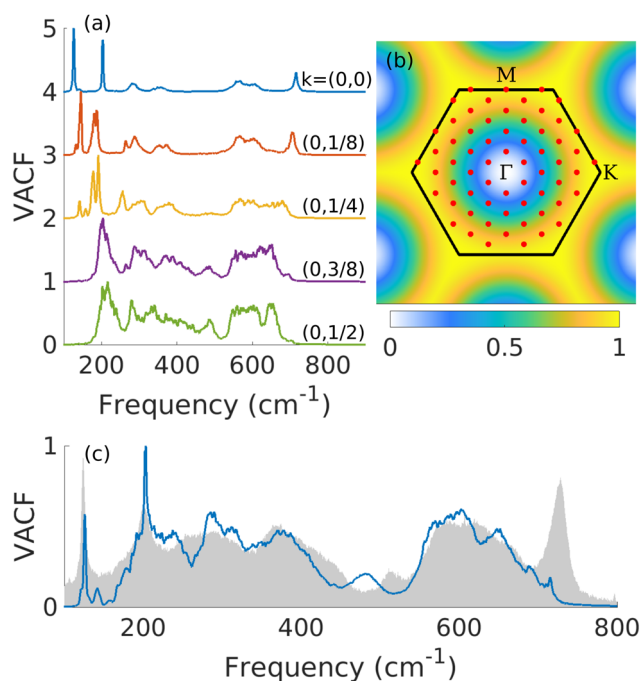


**Fig. 5** (a) Phonon density of states for wavevectors along the  $\Gamma$ -M path. Labels on the right show the coordinates of the wavevector. (b) First Brillouin zone (black lines) with the  $8 \times 8$   $k$ -point mesh (red dots). The colormap represents the weights used in the phonon-projected VACF. (c) Weighted phonon-projected VACF. Modes outside  $\Gamma$  are weighted using the colormap of (b). The gray areas show the experimental Raman spectrum for comparison.



Raman spectra. We identified three peaks that underwent straightforward evolution with the surface composition and thus could also be used to extract the composition from the experimental spectra. Mixed surfaces lead to better agreement in the peak position for some peaks and, importantly, they also reproduce the two broad peaks observed at 300 and 400  $\text{cm}^{-1}$ . Additionally, the modes outside the  $\Gamma$ -point are found to play an important role, which is activated by the disorder such as defects. In particular, modes close to the Brillouin zone edge are found to contribute significantly to the widening of peaks at around 300–400 and 600  $\text{cm}^{-1}$ , as well as the appearance of an additional peak at around 500  $\text{cm}^{-1}$ . Only by including the effect of heterogeneous surfaces and contribution from modes outside the  $\Gamma$ -point, good agreement with the experimentally recorded spectra can be achieved.

## Data availability statement

Data for this paper, including input files, atomic structures, energies and forces of the training set, and MD trajectories are available at Materials Cloud Archive at <https://doi.org/10.24435/materialscloud:w2-g5>.

## Conflicts of interest

There are no conflicts to declare.

## Acknowledgements

We are grateful to the Academy of Finland for support under the Academy Research Fellow funding No. 311058 and Academy Postdoc funding No. 330214. We also thank the CSC-IT Center for Science Ltd for generous grants of computer time.

## References

- M. Naguib, M. W. Barsoum and Y. Gogotsi, *Adv. Mater.*, 2021, **33**, 2103393.
- A. Babak, M. K. Lukatskaya and Y. Gogotsi, *Nat. Rev. Mater.*, 2017, 16098.
- E. Lee and D.-J. Kim, *J. Electrochem. Soc.*, 2019, **167**, 037515.
- A. Iqbal, P. Sambyal and C. M. Koo, *Adv. Funct. Mater.*, 2020, **30**, 2000883.
- M. Naguib, M. Kurtoglu, V. Presser, J. Lu, J. Niu, M. Heon, L. Hultman, Y. Gogotsi and M. W. Barsoum, *Adv. Mater.*, 2011, **23**, 4248–4253.
- O. Mashtalir, M. Naguib, B. Dyatkin, Y. Gogotsi and M. W. Barsoum, *Mater. Chem. Phys.*, 2013, **139**, 147–152.
- C. Shi, M. Beidaghi, M. Naguib, O. Mashtalir, Y. Gogotsi and S. J. L. Billinge, *Phys. Rev. Lett.*, 2014, **112**, 125501.
- H.-W. Wang, M. Naguib, K. Page, D. J. Wesolowski and Y. Gogotsi, *Chem. Mater.*, 2016, **28**, 349–359.
- R. Ibragimova, M. J. Puska and H.-P. Komsa, *ACS Nano*, 2019, **13**, 9171–9181.
- R. Ibragimova, P. Erhart, P. Rinke and H.-P. Komsa, *J. Phys. Chem. Lett.*, 2021, **12**, 2377–2384.
- A. Sarycheva and Y. Gogotsi, *Chem. Mater.*, 2020, **32**, 3480–3488.
- D. B. Lioi, G. Neher, J. E. Heckler, T. Back, F. Mehmood, D. Nepal, R. Pachter, R. Vaia and W. J. Kennedy, *ACS Appl. Nano Mater.*, 2019, **2**, 6087–6091.
- A. Sarycheva, M. Shanmugasundaram, A. Krayev and Y. Gogotsi, *ACS Nano*, 2022, **16**, 6858–6865.
- T. Hu, J. Wang, H. Zhang, Z. Li, M. Hu and X. Wang, *Phys. Chem. Chem. Phys.*, 2015, **17**, 9997–10003.
- T. Hu, M. Hu, B. Gao, W. Li and X. Wang, *J. Phys. Chem. C*, 2018, **122**, 18501–18509.
- L. Lindsay, D. A. Broido and T. L. Reinecke, *Phys. Rev. B: Condens. Matter Mater. Phys.*, 2013, **87**, 165201.
- M. Thomas, M. Brehm, R. Fligg, P. Vöhringer and B. Kirchner, *Phys. Chem. Chem. Phys.*, 2013, **15**, 6608–6622.
- A. Putrino and M. Parrinello, *Phys. Rev. Lett.*, 2002, **88**, 176401.
- Q. Wan, L. Spanu, G. A. Galli and F. Gygi, *J. Chem. Theory Comput.*, 2013, **9**, 4124–4130.
- S. Lubner, M. Iannuzzi and J. Hutter, *J. Chem. Phys.*, 2014, **141**, 094503.
- E. Kocer, T. W. Ko and J. Behler, *Annu. Rev. Phys. Chem.*, 2022, **73**, 163–186.
- J. Behler and M. Parrinello, *Phys. Rev. Lett.*, 2007, **98**, 146401.
- A. P. Bartók, M. C. Payne, R. Kondor and G. Csányi, *Phys. Rev. Lett.*, 2010, **104**, 136403.
- Z. Fan, Z. Zeng, C. Zhang, Y. Wang, K. Song, H. Dong, Y. Chen and T. Ala-Nissila, *Phys. Rev. B*, 2021, **104**, 104309.
- R. Jinnouchi, J. Lahnsteiner, F. Karsai, G. Kresse and M. Bokdam, *Phys. Rev. Lett.*, 2019, **122**, 225701.
- R. Jinnouchi, F. Karsai and G. Kresse, *Phys. Rev. B*, 2019, **100**, 014105.
- A. Hashemi, A. V. Krasheninnikov, M. Puska and H.-P. Komsa, *Phys. Rev. Mater.*, 2019, **3**, 023806.
- S. M. Oliver, J. J. Fox, A. Hashemi, A. Singh, R. L. Cavaleiro, S. Yee, D. W. Snyder, R. Jaramillo, H.-P. Komsa and P. M. Vora, *J. Mater. Chem. C*, 2020, **8**, 5732–5743.
- Z. Kou, A. Hashemi, M. Puska, A. V. Krasheninnikov and H.-P. Komsa, *npj Comput. Mater.*, 2020, **6**, 59.
- P. Sutter, H. Komsa, H. Lu, A. Gruverman and E. Sutter, *Nano Today*, 2021, **37**, 101082.
- G. R. Medders and F. Paesani, *J. Chem. Theory Comput.*, 2015, **11**, 1145–1154.
- G. Placzek, *Rayleigh-streuung und Raman-effekt*, Akademische Verlagsgesellschaft, 1934, vol. 2.
- D. A. Long, *The Raman effect*, John Wiley & Sons: Chichester, England, 2002.
- G. Kresse and J. Furthmüller, *Comput. Mater. Sci.*, 1996, **6**, 15–50.
- G. Kresse and J. Furthmüller, *Phys. Rev. B: Condens. Matter Mater. Phys.*, 1996, **54**, 11169–11186.
- J. P. Perdew, A. Ruzsinszky, G. I. Csonka, O. A. Vydrov, G. E. Scuseria, L. A. Constantin, X. Zhou and K. Burke, *Phys. Rev. Lett.*, 2008, **100**, 136406.
- A. Togo and I. Tanaka, *Scr. Mater.*, 2015, **108**, 1–5.





- 38 M. Walter and M. Moseler, *J. Chem. Theory Comput.*, 2020, **16**, 576–586.
- 39 M. Gajdoš, K. Hummer, G. Kresse, J. Furthmüller and F. Bechstedt, *Phys. Rev. B: Condens. Matter Mater. Phys.*, 2006, **73**, 045112.
- 40 P. Liu, C. Verdi, F. Karsai and G. Kresse, *Phys. Rev. Mater.*, 2021, **5**, 053804.
- 41 M. Bokdam, J. Lahnsteiner and D. D. Sarma, *J. Phys. Chem. C*, 2021, **125**, 21077–21086.
- 42 J. Lahnsteiner and M. Bokdam, *Phys. Rev. B*, 2022, **105**, 024302.
- 43 Y. Xie and P. R. C. Kent, *Phys. Rev. B: Condens. Matter Mater. Phys.*, 2013, **87**, 235441.
- 44 M. Khazaei, A. Ranjbar, M. Arai, T. Sasaki and S. Yunoki, *J. Mater. Chem. C*, 2017, **5**, 2488–2503.
- 45 T. Hu, M. Hu, Z. Li, H. Zhang, C. Zhang, J. Wang and X. Wang, *Phys. Chem. Chem. Phys.*, 2016, **18**, 20256–20260.
- 46 S. Nosé, *J. Chem. Phys.*, 1984, **81**, 511–519.
- 47 N. Shuichi, *Prog. Theor. Phys. Suppl.*, 1991, **103**, 1–46.
- 48 H. Zhang, T. Hu, X. Wang and Y. Zhou, *J. Mater. Sci. Technol.*, 2020, **38**, 205–220.
- 49 R. He, Y. Wan, P. Zhao, P. Guo, Z. Jiang and J. Zheng, *Comput. Theor. Chem.*, 2019, **1150**, 26–39.
- 50 R. Ibragimova, P. Rinke and H.-P. Komsa, *Chem. Mater.*, 2022, **34**, 2896–2906.
- 51 R. Benítez, W. H. Kan, H. Gao, M. O'Neal, G. Proust and M. Radovic, *Acta Mater.*, 2016, **105**, 294–305.
- 52 L. H. Karlsson, J. Birch, J. Halim, M. W. Barsoum and P. O. Å. Persson, *Nano Lett.*, 2015, **15**, 4955–4960.
- 53 X. Sang, Y. Xie, M.-W. Lin, M. Alhabeb, K. L. Van Aken, Y. Gogotsi, P. R. C. Kent, K. Xiao and R. R. Unocic, *ACS Nano*, 2016, **10**, 9193–9200.
- 54 T. S. Mathis, K. Maleski, A. Goad, A. Sarycheva, M. Anayee, A. C. Foucher, K. Hantanasirisakul, C. E. Shuck, E. A. Stach and Y. Gogotsi, *ACS Nano*, 2021, **15**, 6420–6429.
- 55 Y. Tian, M. Ju, Y. Luo, X. Bin, X. Lou and W. Que, *Chem. Eng. J.*, 2022, **446**, 137451.
- 56 P. P. Michałowski, M. Anayee, T. S. Mathis, S. Kozdra, A. Wójcik, K. Hantanasirisakul, I. Jóźwik, A. Piatkowska, M. Moździońek, A. Malinowska, R. Didusko, E. Wierzbicka and Y. Gogotsi, *Nat. Nanotechnol.*, 2022, **17**, 1192–1197.
- 57 M. Cardona and M. Brodsky, *Light Scattering in Solids*, Springer-Verlag, 1982.
- 58 S. Ushioda, *Solid State Commun.*, 1974, **15**, 149–153.
- 59 A. Eckmann, A. Felten, I. Verzhbitskiy, R. Davey and C. Casiraghi, *Phys. Rev. B: Condens. Matter Mater. Phys.*, 2013, **88**, 035426.
- 60 C. Z. Wang, C. T. Chan and K. M. Ho, *Phys. Rev. B: Condens. Matter Mater. Phys.*, 1990, **42**, 11276–11283.
- 61 D.-B. Zhang, T. Sun and R. M. Wentzcovitch, *Phys. Rev. Lett.*, 2014, **112**, 058501.
- 62 T. Sun, D.-B. Zhang and R. M. Wentzcovitch, *Phys. Rev. B: Condens. Matter Mater. Phys.*, 2014, **89**, 094109.

